# Boosting Photon Harvesting in Organic Solar Cells with Highly Oriented Molecular Crystals *via* Graphene−Organic Heterointerface

Sae Byeok Jo,[†] Hyun Ho Kim,[†] Hansol Lee,[†] Boseok Kang,[†] Seongkyu Lee,[†] Myungsun Sim,[†] Min Kim,[†] Wi Hyoung Lee,[‡] and Kilwon Cho*,[†]

[†]Department of Chemical Engineering, Pohang University of Science and Technology, Pohang 790-784, Korea and [‡]Department of Organic and Nano System Engineering, Konkuk University, Seoul 143-701, Korea

ABSTRACT Photon harvesting in organic solar cells is highly dependent on the anisotropic nature of the optoelectronic properties of photoactive materials. Here, we demonstrate an efficient approach to dramatically enhance photon harvesting in planar heterojunction solar cells by using a graphene−organic heterointerface. A large area, residue-free monolayer graphene is inserted at anode interface to serve as an atomically thin epitaxial template for growing highly orientated pentacene crystals with lying-down orientation. This anisotropic orientation enhances the overall optoelectronic properties, including light absorption, charge carrier lifetime, interfacial energetics, and especially the exciton diffusion length. Spectroscopic and crystallographic analysis reveal that the lying-down orientation persists until a thickness of 110 nm, which, along with increased exciton diffusion length up to nearly 100 nm, allows the device optimum thickness to be doubled to yield significantly enhanced light absorption within the photoactive layers. The resultant photovoltaic performance shows simultaneous increment in V_{oc}, J_{sc}, and FF, and consequently a 5 times increment in the maximum power conversion efficiency than the equivalent devices without a graphene layer. The present findings indicate that controlling organic−graphene heterointerface could provide a design strategy of organic solar cell architecture for boosting photon harvesting.
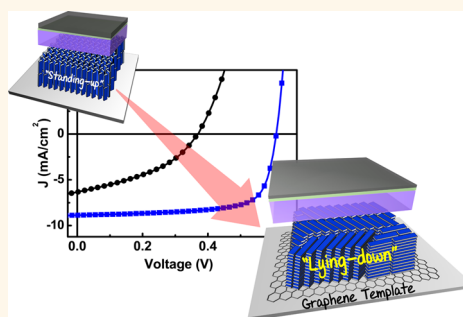
KEYWORDS: organic solar cells · molecular orientation · planar heterojunction · graphene · epitaxial growth · heterointerface

I n the field of organic electronics, the anisotropic nature of the optoelectronic properties of conjugated organic molecules has been investigated as one of the important parameters for the optimization of organic electronic devices.[1−18] Especially, it has been well established that the orientation of conjugated organic molecules determines their electrical properties by governing the overlap of π orbitals in the direction of charge transport.[1−14] For field-effect transistor applications, the molecular planes perpendicular to the substrate is beneficial for the lateral transport of charge carriers through the channel region, which is one of the determinant for the field-effect mobility and resultant device performances.[1] On the other hand, the optical properties of the conjugated molecules are also highly anisotropic depending on the

direction of the transition dipoles. Light−dipole and dipole−dipole interactions among adjacent molecules determine the optical transition and exciton transfer rate,[15] which are key characteristics of optical absorption by organic molecules.[16] The energetic states of excitons and exciplexes (or charge-transfer excitons among heterogeneous molecular interfaces) could also be affected by the molecular orientation because of the different orbital overlap among the molecules.[17,18]

In this sense, it can be easily inferred that controlling the molecular orientation could be an important strategy to optimizing the device performance of organic optoelectronic devices, especially organic solar cells (OSCs), which could provide an efficient renewable energy source by rapid energy payback time.[19] Moreover, since the

small-molecule based OSCs could provide potential advantage over polymer based OSCs due to their greater ease of purifying the materials, the small-molecule based OSCs could be highly feasible for the practical applications and mass-production of the energy devices.[20] Therefore, it is of high necessity that the relationship between molecular orientation and anisotropic photon harvesting behavior should be elucidated, including various aspects of excitonic, optical, electrical and energetic properties of oriented conjugated molecular crystals as well as organic—organic interfaces. However, a successful demonstrations of the OSCs based on orientation-controlled organic semiconductors and the clarification of orientation—photon harvesting relationship have not been reported yet, aside from the approaches that include molecular-specific templates.[21−25]

For this purpose, the use of graphene as an electrode or electrode modifier could be beneficial to optimize the performance of OSCs, considering that the transparency and the conductivity of the graphene enable the graphene to serve as both a transparent electrode and a van der Waals epitaxial growth template of various organic semiconductors. Recently, the exceptional electrical, optical and mechanical properties of graphene have been exploited to develop high-performance electronic devices,[26−28] even on large area, transparent and flexible substrates.[29,30] Moreover, the structural properties of graphene, *i.e.*, the 2D honeycomb lattice of sp^2 hybridized carbon atoms, have been successfully demonstrated their feasibility for the atomically thin molecular template for the epitaxial growth of molecular crystals.[1−4,31,32] However, most of the previous reports that use graphene as an electrode and electrode modifier in OSCs focused on the flexibility and transparency of the graphene and the electrical contact properties such as energy level alignment at charge extraction interfaces.[29,33−36] Several approaches reported partial demonstration of specific optical properties of oriented organic semiconductor films on graphene templates such as optical absorption and exciton dissociation,[2,25,31] but their impact on the performance of OSCs has not been fully elucidated yet.

One of the most widely used approaches to enhance photocurrent generation in OSCs is to employ thin planar heterojunction (PHJ) structure by consecutively depositing charge-selective layers comprising electron donors and electron acceptors. However, despite intensive research efforts, the most significant drawback for the many of most-widely used organic semiconductor is that the exciton diffusion length remains short (∼a few tens of nanometers) in comparison to the optical thickness of organic molecules,[37] which has compelled the utilization of randomly distributed heterojunctions structure (bulk heterojunction, BHJ) with nanoscale phase-separation; their use intrinsically

leads to a high probability of photocurrent loss caused by inevitably frequent charge recombination and misdirected diffusion toward counter electrode. In this regard, recent studies have focused on the development of appropriate vertically phase-separated structure with more distinct donor—acceptor interfaces to reduce the charge recombination and facilitate charge extraction.[38−43] Therefore, a new design strategy of the organic solar architecture for enhancing exciton diffusion properties in photoactive layers has been required to be developed to efficiently convert the absorbed photons to charge carriers by using PHJ structure with distinct carrier selective interfaces.

In the present study, we investigated the impact of molecular orientation control of a model organic semiconductor, pentacene, on the design strategy of OSCs by employing a graphene—organic heterointerface. As reported in previous works,[1−4] the insertion of graphene easily promoted the formation of pentacene crystals in the lying-down orientation by quasi-epitaxial growth. Spectroscopic and crystallographic analyses revealed that the lying-down orientation could persist until a thickness of 110 nm. In comparison to the previous reports on the BHJ OSCs with graphene or graphene-modified electrodes, graphene in our approach not only facilitated the charge transfer at the interfaces but also directly affected the optoelectrical properties of the photoactive layers, which noticeably enhanced OSC performance. The lying-down orientation of the optical transition dipole along the long-axis of pentacene resulted in activation of new absorption energy levels and an overall increment of optical density within the film. Static and spectrally resolved photoluminescence quenching (SR-PLQ) showed highly anisotropic diffusion dynamics of excitons in pentacene crystals, yielding an exciton diffusion length of up to 100 nm for highly oriented pentacene films on graphene, which is almost twice larger value than isotropic crystals. The transient photovoltage (TPV) and photocurrent (TPC) decay measurement also showed that enhanced charge transport in the $\pi-\pi$ stacking direction and facilitated charge extraction at the anode interface significantly increased the lifetime of the photogenerated charge carriers even at a high charge carrier concentration. These characteristics allowed the device optimum thickness to be doubled, generating 50% higher photocurrent than the devices with conventional architecture. Moreover, the interfacial energetics at both the pentacene—anode and pentacene—fullerene interface facilitated the formation of a built-in potential, leading to a higher open circuit voltage (V_{oc}) and fill factor (FF). The resultant photovoltaic performance showed maximum power conversion efficiency which was 5 times that of devices without graphene layers, indicating that orientation control *via* graphene can provide a simple, efficient platform for enhancing the photovoltaic performances of OSCs.
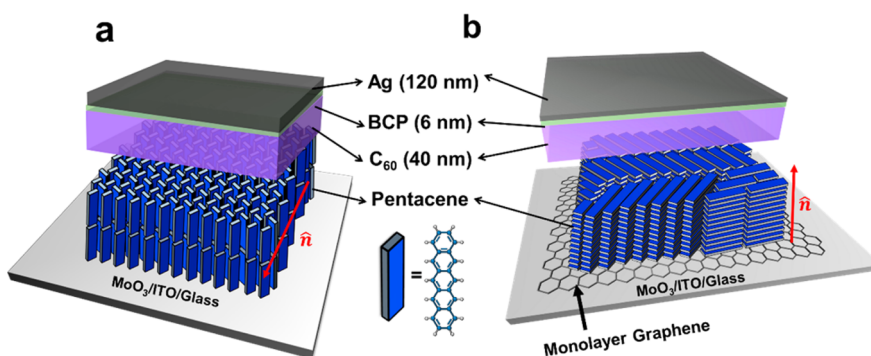
Figure 1. Schematic illustrations of orientation-controlled PHJ OSC devices. (a) Conventional PHJ OSC devices incorporating pentacene as the donor material and C_{60} as the acceptor material. The pentacene molecule adopts the standing-up orientation on the anode surface. (b) The PHJ OSC devices incorporating the graphene monolayer at the anodic interface. The insertion of graphene promotes the quasi-epitaxial growth of pentacene, which adopts a lying-down orientation with its molecular plane parallel to the anode surface.

RESULTS AND DISCUSSION

Figure 1 shows a schematic of PHJ OSCs with a monolayer graphene incorporated. Considering that pentacene molecules preferentially adopt standing-up orientation with herringbone molecular packing on poly-(3,4-ethylenedioxythiophene):poly(styrenesulfonate) (PEDOT:PSS) and on most transparent conducting oxide substrates as illustrated in Figure 1a,[8] the introduction of atomically thin graphene sheets as a molecular template could efficiently alter the growth of pentacene such that it assumes the lying-down orientation on anodic surfaces. In this sense, monolayer graphene grown by chemical vapor deposition (CVD) was transferred onto MoO_3(9 nm)/ITO substrates as an anode modifier *via* water-free wet-transfer method. (Figure S1 in Supporting Information) Owing to the sensitivity of anodic interfacial layer (MoO_3 or PEDOT: PSS) to protic solvents, we used an organic solvent *n*-heptane during the entire transfer process.[30] The residual supporting polymer layer on the transferred graphene was then removed by dipping the substrate in chloroform and thermally annealing under H_2 condition at 350 °C. The resulting substrate had no polymeric residue on top of the graphene surface as observed in the previous report,[1] and the transmittance and resistivity of the anode were maintained satisfactorily after thermal treatment (Figure S5 in Supporting Information). The root-mean-square (RMS) roughness of the substrate was less than 2 nm for all the substrates; 1.88 and 1.58 nm before and after the thermal treatment of MoO_3/ITO, and 1.48 nm for thermally treated graphene/MoO_3/ITO substrates. The cross-section profiles are shown in the Supporting Information. The quality of the CVD grown monolayer graphene was confirmed by Raman spectroscopy. The lack of discernible D-band peak and high 2D/G ratio showed that the high quality of monolayer graphene was preserved after transfer and thermal treatment process on top of MoO_3/ITO substrate (Supporting Information Figure S2). Then, pentacene was thermally

deposited on top of the substrates at a rate of 0.2 Å/s at room temperature. For comparison, the substrate without graphene layer was also studied.

First, the growth modes of pentacene on respective substrates were investigated. To characterize the morphology of grown pentacene films, atomic force microscopy (AFM) was used (Figure 2). Clear differences in the pentacene film topography were observed between the graphene/MoO_3/ITO and MoO_3/ITO substrate. On the MoO_3/ITO substrate, homogeneous nucleation was observed with high density of pentacene nuclei. In comparison to the growth on quartz substrates (Supporting Information Figure S4a), the pentacene grain mainly underwent vertical growth as deposition proceeded, resulting in small grains with a relatively large RMS roughness (±25 nm) in the entire pentacene film at a high thickness (140 nm). The rough surface morphology of the MoO_3/ITO substrate might have prohibited the lateral growth of pentacene, resulting in pentacene film with laterally small grains. By contrast, the insertion of clean graphene at pentacene-anode interface promoted a completely different growth mode of pentacene (Figure 2b). Initially, the pentacene film exhibited fiber-like texture and deep trenches with distinct angle between grains. These characteristics were well maintained for thickness up to 100 nm. The strong interaction between graphene surface and molecular plane of pentacene promoted quasi-epitaxial growth of pentacene despite relatively high roughness of the substrate, as previously reported in the epitaxial growth of pentacene on graphite flakes.[44-46] However, without completely removing the polymeric residue, the pentacene film showed mixed domains of small and fiber-like grains. At higher thicknesses (>140 nm), both pentacene films grown on as-transferred (without thermal treatment) and residue-free graphene showed decline in the grain size which resembled the topography of pentacene film 0pc6on the MoO_3/ITO substrate (Supporting Information Figure S6). The change of the morphology, due to the transition from standing-up to

Pentacene thickness

10nm   50nm   140nm

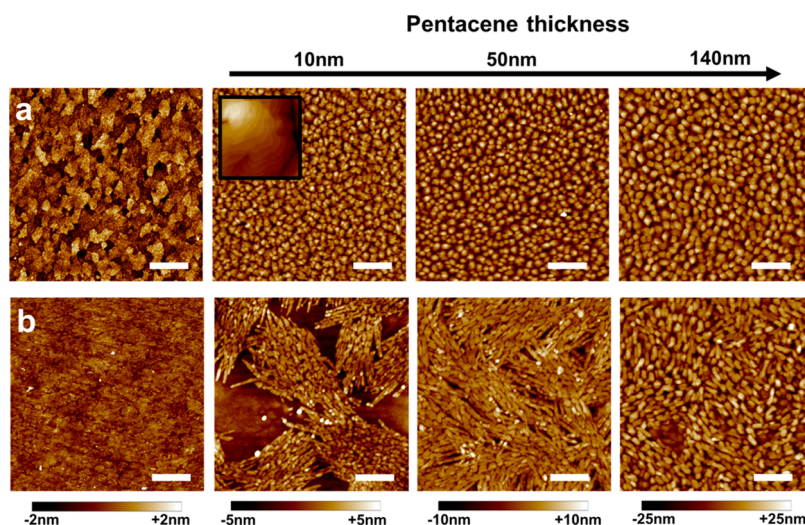-2nm   +2nm   -5nm   +5nm   -10nm   +10nm   -25nm   +25nm

Figure 2. Morphological analysis of the growth of pentacene on the anode surface. AFM images of two different substrates and corresponding pentacene films with varying thickness. Thermally treated (a) MoO₃/ITO substrate and (b) graphene/MoO₃/ITO substrate at 350 °C under H₂ flow in vacuum. The inset image in the second column of (a) shows a magnified morphology. Scale bars: 800 nm.
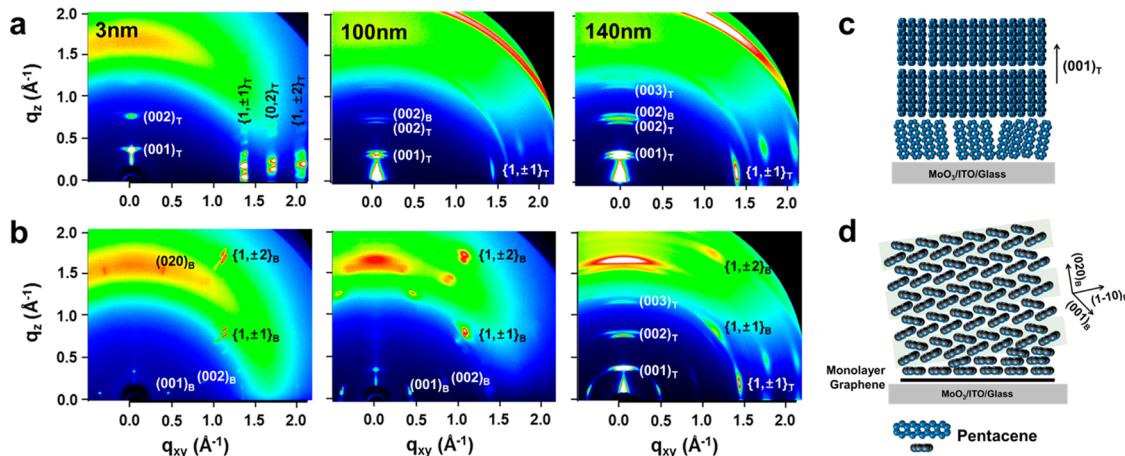

Figure 3. 2D-GIXD of pentacene films with various thicknesses. (a) Pentacene films grown on MoO₃/ITO and (b) graphene/MoO₃/ITO substrates. Schematic representations of the possible molecular packing orientation during the growth of pentacene on (c) MoO₃/ITO and (d) graphene/MoO₃/ITO substrates. The initial growth of pentacene was observed by depositing a pentacene film of 3 nm thickness. The subscripts T and B indicate the thin film and bulk phase of the pentacene crystal, respectively. Parentheses (xyz) indicates the 3-dimensional Miller indices of the crystal lattice planes, while brackets {xy} indicate the 2-dimensional group of Miller indices which correspond to the Bragg rods in a specific crystallographic plane direction.

lying-down crystallographic orientation at high thickness, can be attributed to the thermodynamic stability of the exposed crystallographic planes, where (001) plane has been believed to have to lowest surface energy.[47] It has been well established that the interaction between graphene and pentacene led to the quasi-epitaxial growth of stretched pentacene crystals at a few monolayer thickness, and then the pentacene started to adopt the herringbone structure with slightly tilted crystals as the thickness increased. At higher thicknesses, the high surface energy of exposed (020) plane led to gradual shift in the crystallographic orientation until the uppermost layer of the pentacene adopted the energetically stable orientation with (001) plane normal to the substrate.[47−49]

To clearly understand the crystallographic orientation of pentacene on respective substrates, 2D grazing incidence X-ray diffraction (2D GIXD) patterns were obtained and analyzed[50] (Figure 3). At the initial stage of pentacene growth (3 nm), pentacene on graphene clearly showed (001) and (002) crystal reflections tilted 18° with respect to q_{xy}, as well as (020) and {1,±1} reflections tilted 12° and 40° with respect to q_z, respectively. As deposition proceeded, the (001) reflection on the q_z axis gradually emerged until the diffraction pattern adopted a diffusive ring pattern for the pentacene film with 120 nm thickness. The diffraction pattern and spacing, which are in good agreement with those previously reported for the graphene-templated growth of pentacene

molecules,[51,52] are consistent with a system in which the first few pentacene layers are fully in lying-down orientation, but subsequent layers have a slight tilt of molecular planes because their interaction with graphene is diminished by the interference from underlying pentacene layers.[1] In contrast, pentacene on the MoO_3/ITO substrate exhibited vertically aligned Bragg rod reflections of $\{1,\pm1\}$, $\{0,2\}$, and $\{1,\pm2\}$ at the initial growth stage, indicating highly oriented structures with the (001) plane along the q_{xy} axis. As the thickness increased, the orientation of pentacene also suffered from thermal fluctuations, thereby resulting in broadening of diffraction patterns as well as the emergence of diffraction signals of both thin film and bulk phase crystals. To quantitatively analyze the crystallographic structure, we used 1D GIXD spectra normalized to the thickness of each film.[49,53,54] Supporting Information Figure S9 shows the out-of-plane, in-plane and tilted-plane (72° to the surface normal direction) pattern of pentacene films on the substrate with and without graphene template. The lattice constants in representative crystallographic planes were calculated and agreed well with the previous results, which reported the differences in thin-film, bulk, and c-axis extended structure of the pentacene.[1,49,54] We also used Scherrer's equation to calculate the coherence length (l_c). The average l_c was on the order of 5–10 nm in size, which corresponds to the 5–7 layer coherence of the crystal planes. The relatively low l_c could be attributed to the formation of small grains on hydrophilic oxide substrates as well as the gradual transition of pentacene crystal orientation.[48] The transition of the crystallographic planes were also obvious in 1D GIXD, where the development of (001)T peak in the out-of-plane direction as well as the appearance of $\{1,\pm1\}_T$ Bragg rods in the in-plane direction along with the increasing thickness of pentacene films on graphene showed the obvious formation of standing-up orientation above 100 nm. Moreover, in the direction of $(001)_B$ diffraction for lying-down pentacene (72° tilted to the surface normal direction) showed increment of crystallinity even up until 140 nm in thickness, indicating that the mixture of both lying-down and standing-up orientated pentacene crystals was formed at high thickness.

Since 2D GIXD patterns only represent the crystalline structure of the entire film, surface-sensitive techniques with low-energy X-rays (a few nanometer penetration depth from the surface) are necessary to corroborate the exact progress of pentacene growth.[54,55] Thus, angle-dependent near edge X-ray absorption fine structure (NEXAFS) measurements with *in situ* deposition of pentacene were conducted to accurately assess the transitions in molecular orientation as the pentacene thickness increased. Pentacene and graphene comprise strongly directional σ and π orbitals in sp^2 hybridized conjugated molecular planes, where the transition dipole of $C_{1s} \rightarrow C = C\pi^*$ in pentacene is perpendicular to the molecular plane of pentacene. Therefore, the transitions observed by NEXAFS are highly dependent on the angle of light incidences.[56] As a result, measuring NEXAFS spectra at various beam incidence angles could aid in the assignment of the directionality of molecular planes. Generally, the $C_{1s} \rightarrow C = C\pi^*$ transitions of pentacene generate seven distinctive components caused by the different chemical environment of each carbon atom, ranging from 282 to 287 eV.[54,55] Although the instrumental limitation on the energetic resolution did not provide exact deconvolution into seven features, the most prominent characteristics of π^* transitions (284.22, 285.20, and 285.77 eV) were obviously developed, indicating that our NEXAFS spectra represented the characteristics of anisotropically oriented crystals of pentacene (Supporting Information Figure S12). Moreover, high-energy absorptions near 293 and 300 eV corresponds to the $C_{1s} \rightarrow C - C\sigma^*$ and $C_{1s} \rightarrow C = C\sigma^*$ transition, respectively, and they were also sensitive to the angle of incidence.

For the pentacene films on graphene (Figure 4d,e), varying incident angle from 20° to 90° diminished the $C_{1s} \rightarrow C = C\pi^*$ transition while increasing the $C_{1s} \rightarrow C - C\sigma^*$ and $C_{1s} \rightarrow C = C\sigma^*$ transitions. These trends persisted until a thickness of 110 nm, at which an abrupt angle-insensitive transition from the disordering of pentacene crystals was observed (Supporting Information Figure S11). When a pentacene molecule adopts lying-down configuration, the $C_{1s} \rightarrow C = C\pi^*$ transition dipole is parallel to the surface normal direction of the substrate. In this case, a low angle incidence maximizes the interaction between the probing light and the dipoles so that the absorption shows intensive peaks. Therefore, it can be safely deduced that the lying-own orientation, the molecular orientation of pentacene on graphene, can be preserved until about a thickness of 110 nm. In contrast, pentacene on the MoO_3/ITO substrate (Figure 4c) exhibited high absorption near 284 eV at a light incidence angle of 90° up to a thickness of 170 nm, indicating that the molecular assembly of pentacene spontaneously adopts the standing-up orientation (Supporting Information Figure S10).

Thus far, we have investigated the growth of pentacene and the extent of its orientation on anodic surfaces with and without graphene layer. To address the effect of these characteristics on optoelectrical properties of pentacene, we first measured the optical absorption of the films. Figure 5a shows the UV–vis absorption spectra of pentacene films with different thicknesses on two different substrates. The optical bandgaps of each film were unchanged, with a value of 1.77 eV. However, as the pentacene film thickness increased, the films with the lying-down orientation started to exhibiting distinctive absorption peaks near 343 nm, with an overall increment in the optical
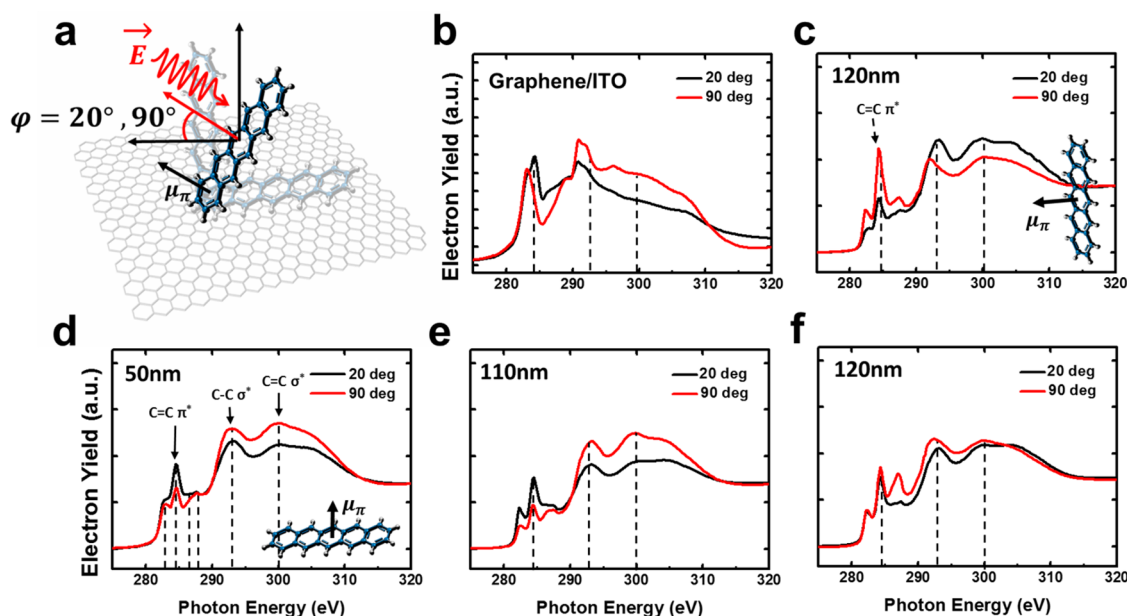
Figure 4. NEXAFS spectra of the pentacene films. (a) Schematic illustration of NEXAFS measurement. Incident angles were defined with respect to the plane direction (20°, nearly parallel to the graphene plane; 90°, normal to the graphene plane). NEXAFS spectra for (b) graphene/MoO$_3$/ITO substrate, (c) pentacene film of 120 nm thickness on the MoO$_3$/ITO substrate, and (d−f) pentacene films on the graphene/MoO$_3$/ITO substrate with various thicknesses. The thicknesses are marked inside each figure. The spectra for other thicknesses can be found in the Supporting Information.

density from 300 to 582 nm. It is well-known that the low-energy peaks near 2.0 eV correspond to the S_0–S_1 vibronic transition, the transition dipole moment of which has B_{1u} symmetry with an orientation perpendicular to the molecular plane.[16] At higher energy (3.7 eV), the S_0-S_3 transition occurs, the dipole moment of which has B_{2u} symmetry, which is along the long axis of the molecules.[56] Therefore, at high energies, the lying-down orientation of pentacene promoted intense absorption by stimulating the unprevailed transitions in the standing-up orientation. Moreover, with increasing thickness, low-energy peaks showed only a slight increment in the pentacene films with the lying-down orientation, which was in good agreement with the postulation that the optical transition was strongly affected by molecular orientation, i.e., the orientation of transition dipoles.

The changes in optical properties described above were quite obvious in the overall optical absorption in the PHJ OSCs. Figure 5b shows the optical simulation results calculated by transfer-matrix methods (described in detail in the Supporting Information). Optical constants were measured using an ellipsometer (Supporting Information Figure S14). An ITO/ MoO$_3$ (9 nm)/pentacene (50, 100 nm)/C$_{60}$ (40 nm)/ bathocuproine (BCP; 6 nm)/Ag (120 nm) structure was employed as the device architecture. The ability of lying-down pentacene to absorb high-energy photons resulted in a significant enhancement in the dissipation profile of the overall optical electric energy inside the pentacene layers at the excitation wavelength of 450 nm. For pentacene films with a standing-up

orientation, the incoming illumination was not dissipated properly inside the pentacene layer; thus, most of the energy was consumed by the following C$_{60}$ layer and the electrode. Moreover, with excitation at 630 nm, comparable energy dissipation was observed in both pentacene films, where pentacene with the lying-down orientation dissipated even a slightly higher energy intensity (Supporting Information Figure S15). Considering the highest intensity of the AM1.5 spectrum of solar illumination near 500 nm, these increments in the optical electric field could significantly contribute to the photocurrent generation of OSCs. Figure 5c shows the calculated photocurrent as a function of pentacene thickness. For pentacene films of 50 nm thickness, maximum achievable photocurrent for the lying-down orientation was approximately 11 mA/cm^2, which is 25% higher than for the standing-up orientation. With increasing thickness, the deviation showed a continuous increment until optical fluctuation occurred near 200 nm. It is clear that the increased absorption capability of lying-down pentacene could boost the photocurrent generation by effectively harvesting incoming photons.

Another interesting feature in the optical properties is exciton dissociation. Since the separation of excitons and consequent generation of charge carriers are determined by the diffusion of excitons to the donor–acceptor heterointerface in OSCs,[57] the short diffusion length of a singlet exciton in pentacene crystals limits the optimum thickness of pentacene down to 50 nm,[58−60] regardless of charge transport. Therefore, increasing the exciton diffusion length up to
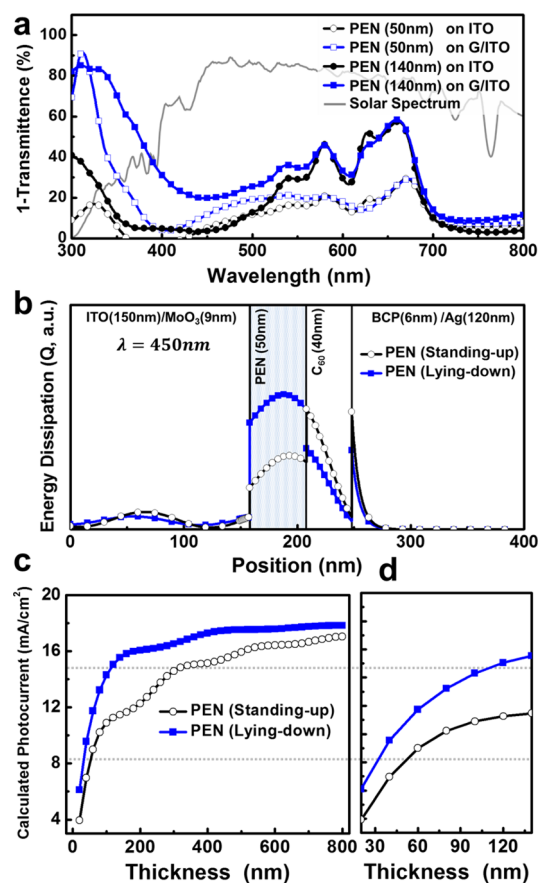
Figure 5. Orientation-dependent light absorption properties of pentacene. (a) UV–Vis absorption spectra of pentacene films on two different substrates at different thicknesses. (b) Optical simulation results describing optical electric field distribution along the thickness direction at the wavelength of 450 nm. The detailed calculations can be found in the Supporting Information. (c) The calculated photocurrents along with the pentacene thickness from 0 to 800 nm and (d) those focused in the range of this experiment (0–140 nm).

the optical thickness of organic semiconductors is detrimental to photon harvesting in OSCs. Intermolecular exciton diffusion can be described by Förster energy transfer, where factors such as exciton lifetime, intermolecular distance, absorption cross section and dipole orientation determine the transfer rate of excitons. It is well-known that, among other transfer pathways, exciton transfer in the $\pi-\pi$ overlap direction is the most prevalent in crystalline conjugated organic molecules.[61] Therefore, if we consider only exciton transfer in the thickness direction, the exciton would have traveled further in the pentacene films with the lying-down orientation than with standing-up orientation. An obvious distinction was observed between the two orientations in the photoluminescence (PL) quenching of pentacene films having 120 nm thickness with a 40 nm C_{60} film as the quenching layer (Figure 6a, Supporting Information Figure S13). With the lying-down orientation, most of the excitons were quenched by the C_{60} layer even for the pentacene film

of 120 nm thickness, while a large portion of the generated excitons in 120 nm pentacene films with the standing-up orientation still remained. This observation was in good agreement with previous reports on the exciton diffusion length in pentacene films.[58−60] Moreover, it can be deduced that exciton migration in the $\pi-\pi$ stacking direction (*i.e.*, lying-down orientation in the thickness direction) can reach up to at least 100 nm without suffering from geminate recombination. To validate our postulation quantitatively, we also conducted spectrally resolved photoluminescence quenching (SR-PLQ) experiments.[59,61] With the use of the 1D steady-state exciton diffusion equation, the absorption coefficient ($\alpha(\lambda)$) and relative PL intensity with blocking (PL_B) and quenching (PL_Q) layers have the following relationship,

$$\eta = \frac{PL_B}{PL_Q} = \alpha(\lambda)L_D + 1 \tag{1}$$

Here, the exciton diffusion length (L_D) corresponds to the slope of η *versus* $\alpha(\lambda)$. We used C_{60} as exciton quenching layer and BCP as the exciton blocking layer on top of the pentacene. The PL intensity was calibrated by the absorption spectra of each film to eliminate the contribution from the quenching and blocking layers. Pentacene films of thickness 110 nm on both graphene and quartz were used to compare the exciton diffusion length, assuming the films were optically thick (exciton density became nearly 0 at the quartz side interface). Figure 6b shows the results of SR-PLQ experiments. L_D was estimated by the slopes in Figure 6b. The L_D of the pentacene film with the standing-up molecular orientation was measured to be 43 nm, which was in agreement with previously reported values.[58−60] However, the exciton diffusion length in the pentacene films with the lying-down orientation was almost double the value for the standing-up orientation, reaching up to 83 nm. This trend confirmed the observed PL quenching efficiency between the two orientations (Figure 6a). Therefore, it can be concluded that, besides the enhanced optical absorption, the increased exciton diffusion guaranteed the utilization of all excitons in pentacene films up to 100 nm thickness, which can significantly enhance photocurrent generation.

To demonstrate OSC devices and their photon harvesting capabilities, we fabricated devices with the following structure: ITO/MoO$_3$ (9 nm)/(graphene)/ pentacene (50/100 nm)/C$_{60}$ (40 nm)/BCP (6 nm)/Ag (120 nm). The optimized devices without graphene layer incorporating pentacene of 50 nm thickness exhibited a power conversion efficiency of 0.85% ($\pm$0.2%) with a V_{oc} of 0.39 V ($\pm$0.01 V), a J_{sc} of 5.8 mA/cm^2 ($\pm$1.1 mA/cm^2) and a FF of 0.38 ($\pm$0.05). As the pentacene thickness was increased up to 100 nm, device performance deteriorated due to increased series resistance, even though photon absorption
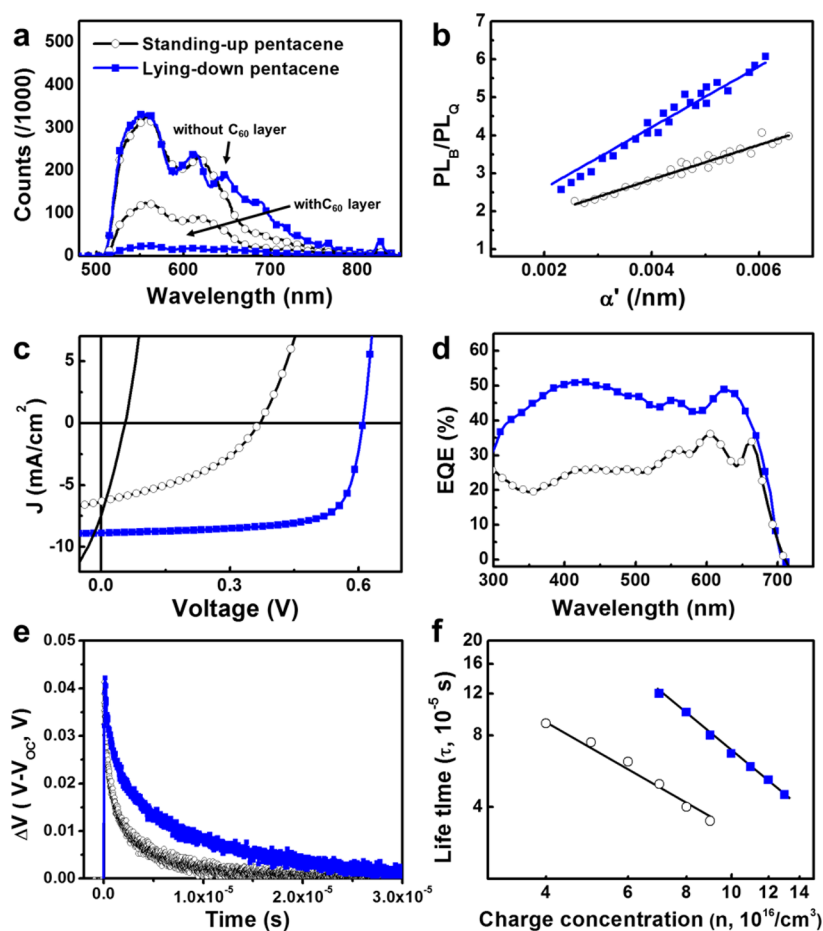
Figure 6. Exciton migration and photovoltaic properties of PHJ OSCs. (a) PL quenching of pentacene (120 nm)/C_{60} (40 nm) films for the standing-up (open circle) and lying-down (blue square) orientations of pentacene in comparison to the PL of the pentacene homo film. PL spectra were measured under the emission mode with excitation at 335 nm. (b) SR-PLQ spectra of pentacene films with different orientations. (c) $J-V$ characteristics of the PHJ OSC devices measured at AM1.5 illumination with an intensity of 100 mW/cm². (d) External quantum efficiency of the OSC devices. (e) Transient photovoltage decay and (f) small-perturbation charge carrier lifetime as a function of the charge concentration within the PHJ OSC devices. PHJ OSC devices in (c−f) were fabricated to have structure of Ag (120 nm)/BCP (6 nm)/pentacene/graphene/MoO_3 (9 nm)/ITO with the lying-down orientation of pentacene (blue square). The devices for the standing-up orientation of pentacene were fabricated with the same structure except for the graphene layer (open circle). The optimum thicknesses of pentacene films were different for the respective orientation (50 nm for standing-up and 100 nm for lying-down orientations). The device for the standing-up orientation of pentacene of thickness 100 nm was also included for comparison (solid line) in (c).

increased. However, devices with graphene layers, *i.e.*, devices having pentacene with lying-down orientation, exhibited a significant enhancement in overall photovoltaic parameters at optimized conditions (100 nm in thickness): a V_{oc} of 0.62 V ($\pm$0.01 V), a J_{sc} of 8.5 mA/cm² ($\pm$1.3 mA/cm²) and a FF of 0.74 ($\pm$0.03) (Figure 6c). The resultant power conversion efficiency was 3.89% ($\pm$0.3%), 4.6 times higher than that of devices without a graphene layer. Twenty devices for each case were fabricated to demonstrate device-to-device variability. As a reference, the devices fabricated with 50 nm pentacene on graphene showed low reproducibility, of which 60% of the fabricated devices exhibited severe leakage. This discrepancy can be attributed to the small grains and the roughness of the lying-down pentacene crystals at low thickness.

For optimized devices, the increased photocurrent are in good agreement with our observations regarding

the optical properties of the highly oriented lying-down pentacene films. Along with the increased absorption capabilities, the enhanced L_D guaranteed efficient usage of absorbed photons at high thickness. Figure 6d shows the external quantum efficiency (EQE) spectra, where an increment in the utilization of high-energy photons near 400 nm was observed, as well as an overall increment in the quantum efficiency in the entire absorption range. The general trend in photocurrent generation is in line with the observed optical properties described above, with a slight discrepancy possibly caused by rough interfaces, series and geometric resistances across the photoactive layers, and low singlet-fission and triplet exciton harvesting efficiencies for pentacene with lying-down orientations.[17]

Interestingly, besides the photocurrent, photovoltage also showed a significant increment. Although the origin of V_{oc} has been a topic of debate, it is generally
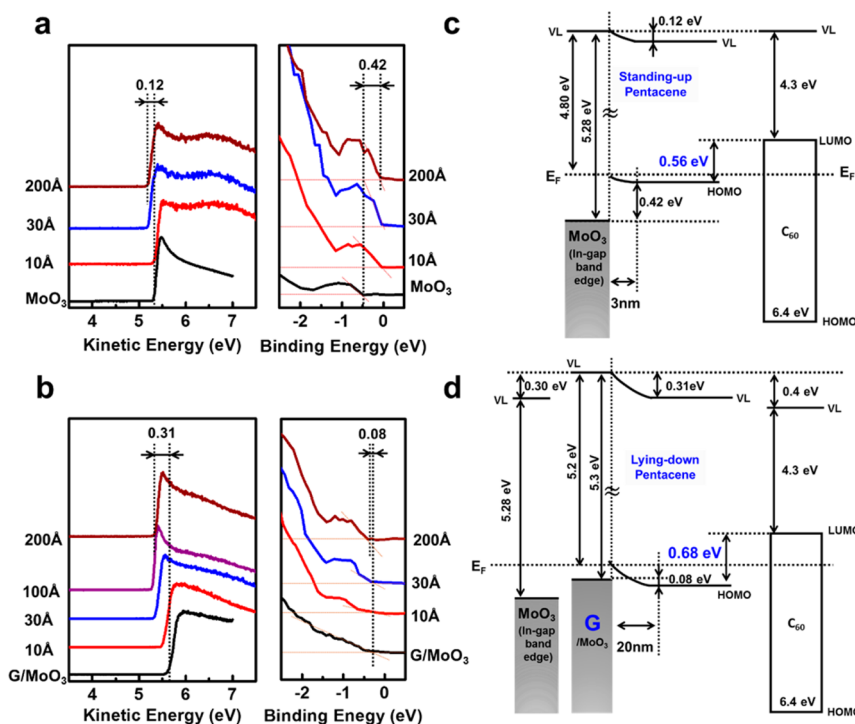
Figure 7. Interfacial energetics incorporating orientation-controlled pentacene films. UPS spectra for the secondary cutoff (left) and valence bands (right) measured under the *in situ* deposition of pentacene on (a) MoO_3/ITO substrate (b) graphene/MoO_3/ITO substrate. The thickness of pentacene is shown at the sides of each figure. Energy level diagrams of (c) pentacene/MoO_3/ITO system and (d) pentacene/graphene/MoO_3/ITO system. Energy levels of C_{60} are shown on the sides. The solid lines indicate the measured energy levels and the dashed lines are inserted as the guidelines for the eyes to compare the energy levels among the materials. VL indicates the vacuum energy level, while E_F indicates the Fermi energy level. The energy level of MoO_3/ITO was drawn on the left side of (d) as a reference.

believed that a difference in the pseudo-Fermi levels of donor and acceptor molecules (ΔE_{DA}) decides the photovoltage as follows,[39,62,63]

$$V_{OC} = \frac{1}{q}\Delta E_{DA} - \frac{n_i kT}{q}\ln\left(\frac{J_{rec}}{J_{ph}}\right) \qquad (2)$$

Here, J_{rec} represents the charge recombination current flowing through the devices. Therefore, to understand the enhancement in V_{oc}, we must consider (i) the interfacial energetics at the donor−acceptor interfaces and (ii) the charge carrier recombination dynamics. Moreover, since the diffusive current near the interface predominantly determines the recombination dynamics near V_{oc},[64,65] it is imperative to characterize the electrode−organic interface.

First, the electronic energy levels of the pentacene films depending on their crystallographic orientations were analyzed by ultraviolet photoemission spectroscopy (UPS)[66−69] under the *in situ* deposition of pentacene. Figure 7 shows the secondary cutoffs and valence band spectra of pentacene. The binding energies were calculated with respect to the vacuum level of the reference Au and the secondary cutoff was measured with −5 V electrical bias to observe the shift in vacuum levels. The detailed experimental and theoretical descriptions are included in the Supporting Information (Figure S14). The HOMO of the MoO_3 on

ITO was measured to be 5.3 eV relative to its vacuum level. Interestingly, despite the deep-lying valence band of MoO_3 (7.9−9.7 eV),[70−72] the thermal treatment of MoO_3 film, which was the same treatment applied to graphene/MoO_3 film to remove the polymeric residue on graphene, induced the formation of widely dispersed in-gap tail states below the Fermi level of the system (Supporting Information Figure S16c). These states comprised oxygen vacancies which led to the partial conversion of the insulating MoO_3 to the conducting MoO_X ($X < 3$), thereby making MoO_3 a feasible hole-selective transport layer for OSCs.[72−75] The pentacene film on MoO_3 film exhibited characteristic features reported on the literature. Wider range spectra of HOMO region are shown in Supporting Information Figure S16. The larger ionization potential of the pentacene films on the graphene/MoO_3/ITO substrate than the pentacene films on MoO_3/ITO substrate with respect to the Fermi level indicated that the smaller electronic polarization energy induced stabilization of photoionization, which corresponded to the lying-down orientation of the pentacene molecules[76,77] as was observed in GIXD and NEXAFS spectra. Therefore, at the MoO_3−pentacene interfaces, the pentacene then formed Schottky barrier of 0.42 eV on the MoO_3/ITO while, at the MoO_3−graphene−pentacene interfaces, pentacene formed Schottky barrier of only

0.08 eV, far closer to an *Ohmic* contact. The difference in the energy level alignment can be attributed to the shift of the graphene Fermi level by the spontaneous donation or acceptance of electrons from each contact, which led to the formation of a stepwise energy level alignment at charge collecting contacts.[78,79] However, despite the clear distinction in injection barriers, this alone cannot explain the difference in V_{oc}, since the diffusional current caused by the band bending at the charge-collecting interface generally compensates for the buildup of extra internal fields at the *Ohmic* contact in PHJ OSCs.[80,81] Therefore, the energetic interface at the donor−acceptor heterojunction should be considered.

For this purpose, pentacene films were further deposited to acquire intrinsic properties of pentacene in different orientations. As deposition proceeded, the shifts in the vacuum level and valence band saturated, indicating that the energy level at the surface of the pentacene film of thickness 20 nm corresponded to the intrinsic properties of the pentacene with specific molecular orientation. Considering both the valence band shifts and vacuum level shifts, the HOMO energy levels of lying-down and standing-up orientation exhibited similar values with respect to their own vacuum level, 4.67 and 4.66 eV. However, due to the difference in the surface dipole moments depending on the crystallographic orientations,[69,76,82] the lying-down pentacene intrinsically induced a noticeable shift in the vacuum level, 0.19 eV lower compared to standing-up pentacene orientation. Therefore, with respect to the intrinsic Fermi energy level and LUMO energy level of fully grown C_{60} films (4.3 eV with respect to the vacuum level), the difference between the HOMO of pentacene and the LUMO of C_{60}, ΔE_{DA}, was 0.68 eV with lying-down orientations of the pentacene and 0.56 with standing-up orientations of the pentacene. Therefore, it can be seen that the increment of photovoltage can be partially attributed to the increased energy level offset at the donor−acceptor interface. Regarding the similar bandgaps of lying-down and standing-up pentacene (Figure 5a), the large differences between the LUMO of the donor and the LUMO of the acceptor, which constitutes the energetic potential for the exciton separation, remained sufficiently large (1.54 and 1.42 eV for standing-up and lying-down, respectively) so that the exciton separation could be affected to a minimal degree, specifically in terms of energetic driving force.

To further address the variation in photovoltaic performance, the nongeminate recombination dynamics of charge carriers were investigated by TPV and TPC measurements. TPV and TPC signals were measured at various illumination intensities (from 40 to 100 mW/cm²) of the AM1.5 spectrum to quantitatively assess the charge carrier lifetime (τ_n) and charge carrier density (n) in the PHJ OSCs. The samples were subjected to 3 ns laser perturbation (532 nm

wavelength) to measure the dynamic photoresponse. The lifetime of charge carriers generated by this small perturbation ($\tau_{\Delta n}$) was calculated by exponential fitting of the photovoltage decay. The recombination order ($\lambda + 1$) was then estimated by the following equation,[83−85]

$$\tau_{\Delta n} = \frac{\tau_0}{1 + \lambda}\left(\frac{1}{n}\right)^\lambda \tag{3}$$

where τ_0 is an experimentally determined constant. Figure 6e shows the transient photovoltage decay profile of PHJ OSCs with and without graphene layer under 1SUN illumination. The $\tau_{\Delta n}$ of charge carriers within the PHJ OSCs incorporating lying-down pentacene was 5.1×10^{-5} s, which is substantially longer than the value of 3.2×10^{-5} s obtained for the devices with standing-up pentacene. The recombination order was estimated by the slope in Figure 6f, which was 2.588 for the PHJ OSCs with lying-down pentacene and 2.198 for the PHJ OSCs with standing-up pentacene. This result indicates that nongeminate recombination within the PHJ OSCs is not dominantly governed by the trap-assisted monomolecular recombination, but also, in large part, influenced by the bimolecular recombination.

Unlike BHJ OSCs, the PHJ OSCs have distinctively separated donor and acceptor layer structures, which allow for the bimolecular recombination of the charge carriers to occur almost exclusively at the donor−acceptor interfaces, since each charge carrier (*i.e.*, holes and electrons) selectively transports through the donor and acceptor layers. In this regard, the higher carrier concentration near the donor−acceptor interface due to the increased exciton diffusion length and enhanced light absorption for pentacene with the lying-down orientation can be attributed to the occurrence of bimolecular recombination in such devices. However, the increased lifetime of charge carriers also indicates that enhanced charge transport caused by the $\pi−\pi$ stacking in charge transport direction and the formation of an *Ohmic* contact at the anodic interface sufficiently suppressed the overall nongeminate charge recombination. In contrast, the PHJ OSCs with pentacene in standing-up orientation had a shorter lifetime and a recombination order higher than 2, even with relatively lower charge carrier generation (Figure 6f). As described in the Supporting Information Figure S17, the hole transport properties measured by space-charge-limited (SCL) current measurement showed at least 2 orders of magnitude higher hole mobility for the pentacene with lying-down orientations than with the standing-up orientations. Since the charge transport in organic semiconductors is determined by the direction and the proximity of the $\pi−\pi$ stacking among molecules as is the exciton transport, pentacene possesses high charge transport anisotropy with which the charge transport along $a−b$ plane is

significantly facilitated in comparison to the charge transport along the c-axis.[45,86] The a–b plane perpendicular to the substrate in lying-down orientated pentacene crystals then resulted in the significantly facilitated hole transport compared to the standing-up oriented crystals which had their c-axis in the direction of charge transport.

Moreover, the dark J–V characteristics in Supporting Information Figure S17 also showed a clear distinction in terms of Ohmic-to-SCL transition behavior, where the devices with the standing-up pentacene exhibited indistinctive (smooth) transition indicating the injection-limited hole extractions. These results revealed that the extraction of charge carriers at each electrode was not sufficiently selective to prevent bimolecular recombination, which could be due to the high hole injection barriers at anodic interface (Figure 7). Therefore, it can be concluded that, besides enhanced optical properties, the lying-down orientation of pentacene also suppresses the charge recombination in PHJ OSC devices, even at high photoactive layer thickness, thereby minimizing the recombination loss of V_{oc}.[80,87] Moreover, considering that FF is mainly determined by the series resistance in PHJ OSCs, this trend in recombination reduction could also account for the significant enhancement in FF (0.38 to 0.74) obtained when pentacene is in the lying-down orientation.

CONCLUSION

In summary, the effects of pentacene orientation on the optical and electrical properties were systematically investigated. The findings demonstrated that an increment in photovoltaic performance can be achieved by controlling the molecular orientation of pentacene. By the insertion of graphene at the anodic interface, the nearly lying-down crystalline orientation of pentacene could be achieved, which enhanced optical transitions, doubled the exciton diffusion, promoted Ohmic contact, and increased the built-in potential of OSC devices. By further exploiting the nature of the quasi-epitaxial growth of conjugated organic molecules on graphene, this approach can give a hint to a wide range of materials and optoelectronic applications. Moreover, the resultant performance enhancement in OSC devices could be useful in developing high-performance OSCs.

EXPERIMENTAL SECTION

Materials and Device Fabrication. For the growth of the graphene monolayer, a copper foil was heated to 1000 °C under H_2 flowing at 10 sccm and 60 mTorr and subsequently at 45 sccm. CH_4 gas was flowed at 300 mTorr for 30 min. The chamber was then rapidly cooled to room temperature under H_2 flowing at 10 sccm. A schematic of the transfer process for CVD-grown graphene is shown in Supporting Information Figure S1. The CVD-grown graphene films on the copper foil were covered with poly(methyl methacrylate) (PMMA, M_w = 340 kg mol^{-1}), and the graphene on the back side of the copper foil was removed using oxygen plasma. This sample was then floated in an aqueous 0.1 M ammonium persulfate solution (($NH_4)_2S_2O_8$). After all of the copper foil was etched away, the graphene film with the PMMA supporting layer was moved to a deionized water bath for 10 min and dried under ambient conditions. The dried PMMA/graphene layers were then transferred to the target substrates; this was followed by the removal of the PMMA support layer with chloroform for 24 h and thermal treatment at 350 °C under H_2, as shown in Supporting Information Figure S1. The devices were fabricated by the consecutive thermal deposition of pentacene (50–100 nm), C_{60} (40 nm), BCP (6 nm) under high-vacuum (<10^{-7} Torr) condition at room temperature. The electrodes were formed by depositing Al (120 nm) through a shadow mask.

Characterization. The graphene films were characterized by Raman spectroscopy at 532 nm (WITec, Micro Raman). Film transmittances were determined using a Varian CARY-500 spectrophotometer under UV–Vis irradiation in the transmittance mode. The morphologies of the pentacene films were determined using an atomic force microscope (Digital Instruments Multimode Nanoscope III) in tapping mode. 2D-GIXD, UPS, and NEXAFS measurements were performed at the 3C, 8A2, and 4D beamlines at Pohang Accelerator Laboratory (PAL) in Korea, respectively. The current–voltage (J–V) characteristics were measured using a Keithley 4200 power source under AM 1.5G illumination at an intensity of 100 mW cm^{-2} (Oriel 1 kW solar simulator) with a PVM 132 reference cell certified by NREL. All electrical measurements and fabrication processes were performed under inert N_2 environment. The incident photon-to-current conversion efficiency was measured using a photomodulation spectroscopy setup (Merlin, Oriel) with monochromatic light from a xenon lamp. The power density of the monochromatic light was calibrated using a Si photodiode certified by the National Institute for Standards and Technology. TPV and TPC were measured using a TDC3054C digital oscilloscope connected with high-speed preamplifiers: SR560 and DHPCA-100. The input impedance for TPV was 100 MΩ to ensure an open circuit. The samples were excited by a 3 ns pulse laser at 532 nm (OBB, NL4300, and OD401) under AM 1.5G illumination at an intensity of 100 mW/cm^2. The measured signals were processed as described elsewhere.

REFERENCES AND NOTES

1. Lee, W. H.; Park, J.; Sim, S. H.; Lim, S.; Kim, K. S.; Hong, B. H.; Cho, K. Surface-Directed Molecular Assembly of Pentacene on Monolayer Graphene for High-Performance Organic Transistors. *J. Am. Chem. Soc.* **2011**, *133*, 4447–4454.
2. Singha Roy, S.; Bindl, D. J.; Arnold, M. S. Templating Highly Crystalline Organic Semiconductors Using Atomic Membranes of Graphene at the Anode/Organic Interface. *J. Phys. Chem. Lett.* **2012**, *3*, 873–878.
3. Jarvinen, P.; Hamalainen, S. K.; Banerjee, K.; Hakkinen, P.; Ijas, M.; Harju, A.; Liljeroth, P. Molecular Self-Assembly on

Graphene on Sio2 and H-Bn Substrates. *Nano Lett.* **2013**, *13*, 3199–3204.

4. Kim, D. H.; Lee, H. S.; Shin, H. J.; Bae, Y. S.; Lee, K. H.; Kim, S. W.; Choi, D.; Choi, J. Y. Graphene Surface Induced Specific Self-Assembly of Poly(3-Hexylthiophene) for Nanohybrid Optoelectronics: From First-Principles Calculation to Experimental Characterizations. *Soft Matter* **2013**, *9*, 5355–5360.

5. Witte, G.; Woll, C. Growth of Aromatic Molecules on Solid Substrates for Applications in Organic Electronics. *J. Mater. Res.* **2004**, *19*, 1889–1916.

6. Sullivan, P.; Jones, T. S.; Ferguson, A. J.; Heutz, S. Structural Templating as a Route to Improved Photovoltaic Performance in Copper Phthalocyanine/Fullerene (C(60)) Heterojunctions. *Appl. Phys. Lett.* **2007**, *91*, 233114.

7. Naito, R.; Toyoshinia, S.; Ohashi, T.; Sakurai, T.; Akimoto, K. Molecular Orientation Control of Phthalocyanine Thin Film by Inserting Pentacene Buffer Layer. *Jpn. J. Appl. Phys.* **2008**, *47*, 1416–1418.

8. Chou, C. T.; Lin, C. H.; Tai, Y.; Liu, C. H. J.; Chen, L. C.; Chen, K. H. Stacking Orientation Mediation of Pentacene and Derivatives for High Open-Circuit Voltage Organic Solar Cells. *J. Phys. Chem. Lett.* **2012**, *3*, 1079–1083.

9. Tumbleston, J. R.; Collins, B. A.; Yang, L. Q.; Stuart, A. C.; Gann, E.; Ma, W.; You, W.; Ade, H. The Influence of Molecular Orientation on Organic Bulk Heterojunction Solar Cells. *Nat. Photonics* **2014**, *8*, 385–391.

10. Kim, J. S.; Park, Y.; Lee, D. Y.; Lee, J. H.; Park, J. H.; Kim, J. K.; Cho, K. Poly(3-Hexylthiophene) Nanorods with Aligned Chain Orientation for Organic Photovoltaics. *Adv. Funct. Mater.* **2010**, *20*, 540–545.

11. Giri, G.; Park, S.; Vosgueritchian, M.; Shulaker, M. M.; Bao, Z. High-Mobility, Aligned Crystalline Domains of Tips-Pentacene with Metastable Polymorphs through Lateral Confinement of Crystal Growth. *Adv. Mater.* **2014**, *26*, 487–493.

12. Diao, Y.; Tee, B. C. K.; Giri, G.; Xu, J.; Kim, D. H.; Becerril, H. A.; Stoltenberg, R. M.; Lee, T. H.; Xue, G.; Mannsfeld, S. C. B.; *et al.* Solution Coating of Large-Area Organic Semiconductor Thin Films with Aligned Single-Crystalline Domains. *Nat. Mater.* **2013**, *12*, 665–671.

13. Zhang, Y.; Diao, Y.; Lee, H.; Mirabito, T. J.; Johnson, R. W.; Puodziukynaite, E.; John, J.; Carter, K. R.; Emrick, T.; Mannsfeld, S. C. B.; *et al.* Intrinsic and Extrinsic Parameters for Controlling the Growth of Organic Single-Crystalline Nanopillars in Photovoltaics. *Nano Lett.* **2014**, *14*, 5547–5554.

14. Kim, D. H.; Park, Y. D.; Jang, Y.; Yang, H.; Kim, Y. H.; Han, J. I.; Moon, D. G.; Park, S.; Chang, T.; Chang, C.; *et al.* Enhancement of Field-Effect Mobility Due to Surface-Mediated Molecular Ordering in Regioregular Polythiophene Thin Film Transistors. *Adv. Funct. Mater.* **2005**, *15*, 77–82.

15. Marciniak, H.; Fiebig, M.; Huth, M.; Schiefer, S.; Nickel, B.; Selmaier, F.; Lochbrunner, S. Ultrafast Exciton Relaxation in Microcrystalline Pentacene Films. *Phys. Rev. Lett.* **2007**, *99*, 176402.

16. Hinderhofer, A.; Heinemeyer, U.; Gerlach, A.; Kowarik, S.; Jacobs, R. M. J.; Sakamoto, Y.; Suzuki, T.; Schreiber, F. Optical Properties of Pentacene and Perfluoropentacene Thin Films. *J. Chem. Phys.* **2007**, *127*, 194705.

17. Lee, J.; Jadhav, P.; Reusswig, P. D.; Yost, S. R.; Thompson, N. J.; Congreve, D. N.; Hontz, E.; Van Voorhis, T.; Baldo, M. A. Singlet Exciton Fission Photovoltaics. *Acc. Chem. Res.* **2013**, *46*, 1300–1311.

18. Shim, H. S.; Kim, H. J.; Kim, J. W.; Kim, S. Y.; Jeong, W. I.; Kim, T. M.; Kim, J. J. Enhancement of near-Infrared Absorption with High Fill Factor in Lead Phthalocyanine-Based Organic Solar Cells. *J. Mater. Chem.* **2012**, *22*, 9077–9081.

19. Darling, S. B.; You, F. The Case for Organic Photovoltaics. *RSC Adv.* **2013**, *3*, 17633–17648.

20. Nikiforov, M. P.; Lai, B.; Chen, W.; Chen, S.; Schaller, R. D.; Strzalka, J.; Maser, J.; Darling, S. B. Detection and Role of Trace Impurities in High-Performance Organic Solar Cells. *Energy Environ. Sci.* **2013**, *6*, 1513–1520.

21. Kim, S.-Y.; Jeong, W.-I.; Mayr, C.; Park, Y.-S.; Kim, K.-H.; Lee, J.-H.; Moon, C.-K.; Brütting, W.; Kim, J.-J. Organic Light-Emitting Diodes with 30% External Quantum Efficiency Based on a Horizontally Oriented Emitter. *Adv. Funct. Mater.* **2013**, *23*, 3896–3900.

22. Yi, Y.; Coropceanu, V.; Brédas, J.-L. Exciton-Dissociation and Charge-Recombination Processes in Pentacene/C60 Solar Cells: Theoretical Insight into the Impact of Interface Geometry. *J. Am. Chem. Soc.* **2009**, *131*, 15777–15783.

23. Ayzner, A. L.; Nordlund, D.; Kim, D.-H.; Bao, Z.; Toney, M. F. Ultrafast Electron Transfer at Organic Semiconductor Interfaces: Importance of Molecular Orientation. *J. Phys. Chem. Lett.* **2015**, *6*, 6–12.

24. Lu, X.; Hlaing, H.; Nam, C.-Y.; Yager, K. G.; Black, C. T.; Ocko, B. M. Molecular Orientation and Performance of Nanoimprinted Polymer-Based Blend Thin Film Solar Cells. *Chem. Mater.* **2015**, *27*, 60–66.

25. Zhang, L.; Roy, S. S.; Hamers, R. J.; Arnold, M. S.; Andrew, T. L. Molecular Orientation-Dependent Interfacial Energetics and Built-in Voltage Tuned by a Template Graphene Monolayer. *J. Phys. Chem. C* **2015**, *119*, 45–54.

26. Balog, R.; Jorgensen, B.; Nilsson, L.; Andersen, M.; Rienks, E.; Bianchi, M.; Fanetti, M.; Laegsgaard, E.; Baraldi, A.; Lizzit, S.; *et al.* Bandgap Opening in Graphene Induced by Patterned Hydrogen Adsorption. *Nat. Mater.* **2010**, *9*, 315–319.

27. Wu, Y. Q.; Lin, Y. M.; Bol, A. A.; Jenkins, K. A.; Xia, F. N.; Farmer, D. B.; Zhu, Y.; Avouris, P. High-Frequency, Scaled Graphene Transistors on Diamond-Like Carbon. *Nature* **2011**, *472*, 74–78.

28. Jo, S. B.; Park, J.; Lee, W. H.; Cho, K.; Hong, B. H. Large-area graphene synthesis and its application to interface-engineered field effect transistors. *Solid State Commun.* **2012**, *152*, 1350–1358.

29. Lee, W. H.; Park, J.; Sim, S. H.; Jo, S. B.; Kim, K. S.; Hong, B. H.; Cho, K. Transparent Flexible Organic Transistors Based on Monolayer Graphene Electrodes on Plastic. *Adv. Mater.* **2011**, *23*, 1752–1756.

30. Kim, H. H.; Chung, Y.; Lee, E.; Lee, S. K.; Cho, K. Water-Free Transfer Method for Cvd-Grown Graphene and Its Application to Flexible Air-Stable Graphene Transistors. *Adv. Mater.* **2014**, *26*, 3213–3217.

31. Hong, G.; Wu, Q. H.; Ren, J. G.; Wang, C. D.; Zhang, W. J.; Lee, S. T. Recent Progress in Organic Molecule/Graphene Interfaces. *Nano Today* **2013**, *8*, 388–402.

32. Hong, Y. J.; Yang, J. W.; Lee, W. H.; Ruoff, R. S.; Kim, K. S.; Fukui, T. Van Der Waals Epitaxial Double Heterostructure: Inas/Single-Layer Graphene/Inas. *Adv. Mater.* **2013**, *25*, 6847–6853.

33. Kim, D.; Lee, D.; Lee, Y.; Jeon, D. Y. Work-Function Engineering of Graphene Anode by Bis(Trifluoromethanesulfonyl)Amide Doping for Efficient Polymer Light-Emitting Diodes. *Adv. Funct. Mater.* **2013**, *23*, 5049–5055.

34. Li, S.-S.; Tu, K.-H.; Lin, C.-C.; Chen, C.-W.; Chhowalla, M. Solution-Processable Graphene Oxide as an Efficient Hole Transport Layer in Polymer Solar Cells. *ACS Nano* **2010**, *4*, 3169–3174.

35. Liu, Z.; Parvez, K.; Li, R.; Dong, R.; Feng, X.; Müllen, K. Transparent Conductive Electrodes from Graphene/Pedot:Pss Hybrid Inks for Ultrathin Organic Photodetectors. *Adv. Mater.* **2015**, *27*, 669–675.

36. Yin, Z.; Zhu, J.; He, Q.; Cao, X.; Tan, C.; Chen, H.; Yan, Q.; Zhang, H. Graphene-Based Materials for Solar Cell Applications. *Adv. Energy Mater.* **2014**, *4*, 1300574.

37. Chen, L. M.; Hong, Z. R.; Li, G.; Yang, Y. Recent Progress in Polymer Solar Cells: Manipulation of Polymer: Fullerene Morphology and the Formation of Efficient Inverted Polymer Solar Cells. *Adv. Mater.* **2009**, *21*, 1434–1449.

38. Mora-Sero, I.; Bertoluzzi, L.; Gonzalez-Pedro, V.; Gimenez, S.; Fabregat-Santiago, F.; Kemp, K. W.; Sargent, E. H.; Bisquert, J. Selective Contacts Drive Charge Extraction in Quantum Dot Solids *via* Asymmetry in Carrier Transfer Kinetics. *Nat. Commun.* **2013**, *4*, 2272.

39. Sim, M.; Kim, J. S.; Shim, C.; Cho, K. Cascade Organic Solar Cells with Energy-Level-Matched Three Photon-Harvesting Layers. *Chem. Phys. Lett.* **2013**, *557*, 88–91.

40. Kim, M.; Kim, J. H.; Choi, H. H.; Park, J. H.; Jo, S. B.; Sim, M.; Kim, J. S.; Jinnai, H.; Park, Y. D.; Cho, K. Electrical Performance of Organic Solar Cells with Additiveassisted Vertical Phase Separation in the Photoactive Layer. *Adv. Energy Mater.* **2014**, *4*, 1300612.

41. Yang, B.; Yuan, Y. B.; Huang, J. S. Reduced Bimolecular Charge Recombination Loss in Thermally Annealed Bilayer Heterojunction Photovoltaic Devices with Large External Quantum Efficiency and Fill Factor. *J. Phys. Chem. C* **2014**, *118*, 5196–5202.

42. Chen, D.; Liu, F.; Wang, C.; Nakahara, A.; Russell, T. P. Bulk Heterojunction Photovoltaic Active Layers *via* Bilayer Interdiffusion. *Nano Lett.* **2011**, *11*, 2071–2078.

43. Huang, Y.-C; Welch, G. C.; Bazan, G. C.; Chabinyc, M. L.; Su, W.-F. Self-Vertical Phase Separation Study of Nanoparticle/Polymer Solar Cells by Introducing Fluorinated Small Molecules. *Chem. Commun.* **2012**, *48*, 7250–7252.

44. Forrest, S. R. Ultrathin Organic Films Grown by Organic Molecular Beam Deposition and Related Techniques. *Chem. Rev.* **1997**, *97*, 1793–1896.

45. Koch, N.; Vollmer, A.; Salzmann, I.; Nickel, B.; Weiss, H.; Rabe, J. P. Evidence for Temperature-Dependent Electron Band Dispersion in Pentacene. *Phys. Rev. Lett.* **2006**, *96*, 156803.

46. Harada, Y.; Ozaki, H.; Ohno, K. Selective Observation of Outermost Surface Layer During Epitaxial Growth by Penning-Ionization Electron Spectroscopy: Pentacene on Graphite. *Phys. Rev. Lett.* **1984**, *52*, 2269–2272.

47. Ruiz, R.; Choudhary, D.; Nickel, B.; Toccoli, T.; Chang, K.-C.; Mayer, A. C.; Clancy, P.; Blakely, J. M.; Headrick, R. L.; Iannotta, S.; *et al.* Pentacene Thin Film Growth. *Chem. Mater.* **2004**, *16*, 4497–4508.

48. Nguyen, N. N.; Jo, S. B.; Lee, S. K.; Sin, D. H.; Kang, B.; Kim, H. H.; Lee, H.; Cho, K. Atomically Thin Epitaxial Template for Organic Crystal Growth Using Graphene with Controlled Surface Wettability. *Nano Lett.* **2015**, *15*, 2474–2484.

49. Kim, K.; Santos, E. J. G.; Lee, T. H.; Nishi, Y.; Bao, Z. Epitaxially Grown Strained Pentacene Thin Film on Graphene Membrane. *Small* **2015**, *11*, 2037–2043.

50. Chen, W.; Nikiforov, M. P.; Darling, S. B. Morphology Characterization in Organic and Hybrid Solar Cells. *Energy Environ. Sci.* **2012**, *5*, 8045–8074.

51. Casalis, L.; Danisman, M. F.; Nickel, B.; Bracco, G.; Toccoli, T.; Iannotta, S.; Scoles, G. Hyperthermal Molecular Beam Deposition of Highly Ordered Organic Thin Films. *Phys. Rev. Lett.* **2003**, *90*, 206101.

52. Mattheus, C. C.; Dros, A. B.; Baas, J.; Meetsma, A.; de Boer, J. L.; Palstra, T. T. M. Polymorphism in Pentacene. *Acta Crystallogr., Sect. C: Cryst. Struct. Commun.* **2001**, *57*, 939–941.

53. Hinderhofer, A.; Gerlach, A.; Broch, K.; Hosokai, T.; Yonezawa, K.; Kato, K.; Kera, S.; Ueno, N.; Schreiber, F. Geometric and Electronic Structure of Templated C60 on Diindenoperylene Thin Films. *J. Phys. Chem. C* **2013**, *117*, 1053–1058.

54. Götzen, J.; Käfer, D.; Wöll, C.; Witte, G. Growth and Structure of Pentacene Films on Graphite: Weak Adhesion as a Key for Epitaxial Film Growth. *Phys. Rev. B: Condens. Matter Mater. Phys.* **2010**, *81*, 085440.

55. Kafer, D.; Ruppel, L.; Witte, G. Growth of Pentacene on Clean and Modified Gold Surfaces. *Phys. Rev. B: Condens. Matter Mater. Phys.* **2007**, *75*, 085309.

56. Anger, F.; Osso, J. O.; Heinemeyer, U.; Broch, K.; Scholz, R.; Gerlach, A.; Schreiber, F. Photoluminescence Spectroscopy of Pure Pentacene, Perfluoropentacene, and Mixed Thin Films. *J. Chem. Phys.* **2012**, *136*, 054701.

57. Chen, W.; Xu, T.; He, F.; Wang, W.; Wang, C.; Strzalka, J.; Liu, Y.; Wen, J.; Miller, D. J.; Chen, J.; *et al.* Hierarchical Nanomorphologies Promote Exciton Dissociation in Polymer/Fullerene Bulk Heterojunction Solar Cells. *Nano Lett.* **2011**, *11*, 3707–3713.

58. Najafov, H.; Lee, B.; Zhou, Q.; Feldman, L. C.; Podzorov, V. Observation of Long-Range Exciton Diffusion in Highly Ordered Organic Semiconductors. *Nat. Mater.* **2010**, *9*, 938–943.

59. Lunt, R. R.; Benziger, J. B.; Forrest, S. R. Relationship between Crystalline Order and Exciton Diffusion Length in Molecular Organic Semiconductors. *Adv. Mater.* **2010**, *22*, 1233–1236.

60. Yoo, S.; Potscavage, W. J.; Domercq, B.; Han, S. H.; Li, T. D.; Jones, S. C.; Szoszkiewicz, R.; Levi, D.; Riedo, E.; Marder, S. R.; *et al.* Analysis of Improved Photovoltaic Properties of Pentacene/C-60 Organic Solar Cells: Effects of Exciton Blocking Layer Thickness and Thermal Annealing. *Solid-State Electron.* **2007**, *51*, 1367–1375.

61. Sim, M.; Shin, J.; Shim, C.; Kim, M.; Jo, S. B.; Kim, J. H.; Cho, K. Dependence of Exciton Diffusion Length on Crystalline Order in Conjugated Polymers. *J. Phys. Chem. C* **2014**, *118*, 760–766.

62. Koster, L. J. A.; Mihailetchi, V. D.; Blom, P. W. M. Bimolecular Recombination in Polymer/Fullerene Bulk Heterojunction Solar Cells. *Appl. Phys. Lett.* **2006**, *88*, 052104.

63. Cowan, S. R.; Roy, A.; Heeger, A. J. Recombination in Polymer-Fullerene Bulk Heterojunction Solar Cells. *Phys. Rev. B: Condens. Matter Mater. Phys.* **2010**, *82*, 245207.

64. Servaites, J. D.; Ratner, M. A.; Marks, T. J. Organic Solar Cells: A New Look at Traditional Models. *Energy Environ. Sci.* **2011**, *4*, 4410–4422.

65. Jo, S. B.; Lee, J. H.; Sim, M.; Kim, M.; Park, J. H.; Choi, Y. S.; Kim, Y.; Ihn, S. G.; Cho, K. High Performance Organic Photovoltaic Cells Using Polymer-Hybridized Zno Nanocrystals as a Cathode Interlayer. *Adv. Energy Mater.* **2011**, *1*, 690–698.

66. Ishii, H.; Sugiyama, K.; Ito, E.; Seki, K. Energy Level Alignment and Interfacial Electronic Structures at Organic/Metal and Organic/Organic Interfaces. *Adv. Mater.* **1999**, *11*, 605–625.

67. Heimel, G.; Salzmann, I.; Duhm, S.; Rabe, J. P.; Koch, N. Intrinsic Surface Dipoles Control the Energy Levels of Conjugated Polymers. *Adv. Funct. Mater.* **2009**, *19*, 3874–3879.

68. Cahen, D.; Kahn, A. Electron Energetics at Surfaces and Interfaces: Concepts and Experiments. *Adv. Mater.* **2003**, *15*, 271–277.

69. Duhm, S.; Heimel, G.; Salzmann, I.; Glowatzki, H.; Johnson, R. L.; Vollmer, A.; Rabe, J. P.; Koch, N. Orientation-Dependent Ionization Energies and Interface Dipoles in Ordered Molecular Assemblies. *Nat. Mater.* **2008**, *7*, 326–332.

70. Werfel, F.; Minni, E. Photoemission Study of the Electronic Structure of Mo and Mo Oxides. *J. Phys. C: Solid State Phys.* **1983**, *16*, 6091–6100.

71. Meyer, J.; Shu, A.; Kröger, M.; Kahn, A. Effect of Contamination on the Electronic Structure and Hole-Injection Properties of Moo3/Organic Semiconductor Interfaces. *Appl. Phys. Lett.* **2010**, *96*, 133308.

72. Hammond, S. R.; Meyer, J.; Widjonarko, N. E.; Ndione, P. F.; Sigdel, A. K.; Garcia, A.; Miedaner, A.; Lloyd, M. T.; Kahn, A.; Ginley, D. S.; *et al.* Low-Temperature, Solution-Processed Molybdenum Oxide Hole-Collection Layer for Organic Photovoltaics. *J. Mater. Chem.* **2012**, *22*, 3249–3254.

73. Battaglia, C.; Yin, X.; Zheng, M.; Sharp, I. D.; Chen, T.; McDonnell, S.; Azcatl, A.; Carraro, C.; Ma, B.; Maboudian, R.; *et al.* Hole Selective Moox Contact for Silicon Solar Cells. *Nano Lett.* **2014**, *14*, 967–971.

74. Meyer, J.; Kidambi, P. R.; Bayer, B. C.; Weijtens, C.; Kuhn, A.; Centeno, A.; Pesquera, A.; Zurutuza, A.; Robertson, J.; Hofmann, S. Metal Oxide Induced Charge Transfer Doping and Band Alignment of Graphene Electrodes for Efficient Organic Light Emitting Diodes. *Sci. Rep.* **2014**, *4*, 5380.

75. Tseng, Y.-C.; Mane, A. U.; Elam, J. W.; Darling, S. B. Ultrathin Molybdenum Oxide Anode Buffer Layer for Organic Photovoltaic Cells Formed Using Atomic Layer Deposition. *Sol. Energy Mater. Sol. Cells* **2012**, *99*, 235–239.

76. Fukagawa, H.; Yamane, H.; Kataoka, T.; Kera, S.; Nakamura, M.; Kudo, K.; Ueno, N. Origin of the Highest Occupied Band Position in Pentacene Films from Ultraviolet Photoelectron Spectroscopy: Hole Stabilization *versus* Band Dispersion. *Phys. Rev. B: Condens. Matter Mater. Phys.* **2006**, *73*, 245310.

77. Ellis, T. S.; Park, K. T.; Hulbert, S. L.; Ulrich, M. D.; Rowe, J. E. Influence of Substrate Temperature on Epitaxial Copper Phthalocyanines Studied by Photoemission Spectroscopy. *J. Appl. Phys.* **2004**, *95*, 982–988.

78. Berke, K.; Tongay, S.; McCarthy, M. A.; Rinzler, A. G.; Appleton, B. R.; Hebard, A. F. Current Transport across the Pentacene/Cvd-Grown Graphene Interface for Diode Applications. *J. Phys.: Condens. Matter* **2012**, *24*, 255802.

79. Byun, K. E.; Chung, H. J.; Lee, J.; Yang, H.; Song, H. J.; Heo, J.; Seo, D. H.; Park, S.; Hwang, S. W.; Yoo, I.; *et al.* Graphene for True Ohmic Contact at Metal-Semiconductor Junctions. *Nano Lett.* **2013**, *13*, 4001–4005.

80. Foertig, A.; Wagenpfahl, A.; Gerbich, T.; Cheyns, D.; Dyakonov, V.; Deibel, C. Nongeminate Recombination in Planar and Bulk Heterojunction Organic Solar Cells. *Adv. Energy Mater.* **2012**, *2*, 1483–1489.

81. Cheyns, D.; Poortmans, J.; Heremans, P.; Deibel, C.; Verlaak, S.; Rand, B. P.; Genoe, J. Analytical Model for the Open-Circuit Voltage and Its Associated Resistance in Organic Planar Heterojunction Solar Cells. *Phys. Rev. B: Condens. Matter Mater. Phys.* **2008**, *77*, 165332.

82. Chen, W.; Qi, D.-C.; Huang, H.; Gao, X.; Wee, A. T. S. Organic–Organic Heterojunction Interfaces: Effect of Molecular Orientation. *Adv. Funct. Mater.* **2011**, *21*, 410–424.

83. Credgington, D.; Hamilton, R.; Atienzar, P.; Nelson, J.; Durrant, J. R. Non-Geminate Recombination as the Primary Determinant of Open-Circuit Voltage in Polythiophene: Fullerene Blend Solar Cells: An Analysis of the Influence of Device Processing Conditions. *Adv. Funct. Mater.* **2011**, *21*, 2744–2753.

84. Bisquert, J.; Garcia-Belmonte, G. On Voltage, Photovoltage, and Photocurrent in Bulk Heterojunction Organic Solar Cells. *J. Phys. Chem. Lett.* **2011**, *2*, 1950–1964.

85. Credgington, D.; Durrant, J. R. Insights from Transient Optoelectronic Analyses on the Open-Circuit Voltage of Organic Solar Cells. *J. Phys. Chem. Lett.* **2012**, *3*, 1465–1478.

86. Zheng, Y.; Wee, A. T. S.; Troadec, C.; Chandrasekhar, N. Temperature-Dependent Transition from Injection-Limited to Space-Charge-Limited Current in Metal-Organic Diodes. *Appl. Phys. Lett.* **2009**, *95*, 143303.

87. Li, C.-Z.; Chang, C.-Y.; Zang, Y.; Ju, H.-X.; Chueh, C.-C.; Liang, P.-W.; Cho, N.; Ginger, D. S.; Jen, A. K. Y. Suppressed Charge Recombination in Inverted Organic Photovoltaics *via* Enhanced Charge Extraction by Using a Conductive Fullerene Electron Transport Layer. *Adv. Mater.* **2014**, *26*, 6262–6267.